Journal of Materials Chemistry A

PAPER

View Article Online
View Journal | View Issue

Cite this: J. Mater. Chem. A, 2017, 5, 23620

In situ nitrogen-doped mesoporous carbon nanofibers as flexible freestanding electrodes for high-performance supercapacitors†

Jian Tan,[a] Yulai Han,*[cd] Liang He,[a] Yixiao Dong,[a] Xu Xu,[a] Dongna Liu,[a] Haowu Yan,[a] Qiang Yu,[a] Congyun Huang[a] and Liqiang Mai *[ab]

Received 9th August 2017
Accepted 17th October 2017

DOI: 10.1039/c7ta07024a

rsc.li/materials-a

Herein we propose a low-cost, one-step synthesis of magnesium hydroxide ($Mg(OH)_2$) that is deposited on polyacrylonitrile (PAN) nanofibers by electrospinning. Following carbonization and etching, an *in situ* N-doped mesoporous carbon nanofiber (N-MCNF) network is synthesized. The synthesized flexible network is employed as a freestanding electrode for supercapacitors. The as-constructed supercapacitor based on the N-MCNFs prepared at 900 °C (N-MCNFs-900) can deliver excellent performance with an ultrahigh specific capacitance of 327.3 F g^{-1} at a current density of 1.0 A g^{-1}, and remarkable cycling stability, *e.g.*, only about 7% loss after 10 000 cycles at a constant high charging–discharging current of 20 A g^{-1} in 6 M KOH aqueous electrolyte. The flexible network consisting of N-MCNFs-900 as the electrode material with long cycling stability is highly promising for next-generation high-performance supercapacitors.

1. Introduction

To meet the fast-developing energy demands of the modern society, more novel, green and efficient energy storage devices have been explored.[1–4] Among them, supercapacitors have been receiving rapidly growing attention, owing to their unique advantages, such as high specific power density, fast charge–discharge rates and long cycling stability compared with traditional secondary batteries.[5,6] Electrochemical double-layer capacitors (EDLCs), also known as ultracapacitors or supercapacitors,[7] store charge and release energy based on the fundamental mechanism of reversible adsorption of ions from an electrolyte to high accessible surface area porous carbon electrodes, thus allowing the formation of oppositely charged layers at the electrolyte/electrode interface.[8–10] Generally, the critical issue in the development of supercapacitors is the realization of ideal electrode materials, which possess high conductivity, large ion-accessible specific surface area (SSA) and appropriate pore size distribution.[11,12] Carbon-based supercapacitors display excellent properties of light weight, low cost and bipolar operational flexibility.[13] Therefore, carbon-based materials, including activated carbon (AC),[14] carbon nanofibers,[15,16] carbon nanotubes (CNTs),[17,18] carbon spheres,[19–21] carbon papers[22] and graphene,[23] have been widely employed as electrode materials in supercapacitors. To improve the performance of carbon-based materials, considerable efforts have been made including surface modification and introduction of defects and heteroatoms, such as N,[24–27] B,[28,29] S,[30,31] or P,[32] which can modify the surface chemical functionalities and electronic properties, and greatly increase the capacity of supercapacitors.[33] Among them, N-doping could be the most promising approach to enhance the capacity and obtain superior cycling stability through improving the electrical conductivity and providing more additional active sites.[34,35] Moreover, extensive research efforts have been made to achieve pseudocapacitive redox reactions in mesoporous carbon materials[13,36,37] by carbonizing precursors with suitable templates[13] and conducting polymers with N doping.[38] Nevertheless, these synthesis methods are obviously laborious, expensive and time-consuming.

Herein, an *in situ* MgO template method to synthesize nitrogen-doped mesoporous carbon nanofibers (N-MCNFs) with a polyacrylonitrile (PAN) polymer solution as a precursor is presented. The proposed facile, low-cost process is convenient to prepare N-MCNFs with high SSA, homogeneous pore size distribution and abundant surface functional groups, which shows great potential for carbon-based supercapacitors. It is well known that PAN is a typical hydrocarbon that is used to obtain carbonaceous materials.[39,40] In addition, PAN has a high nitrogen content according to its chemical formula ($(C_3H_3N)_n$),

[a]State Key Laboratory of Advanced Technology for Materials Synthesis and Processing, International School of Materials Science and Engineering, Wuhan University of Technology, Wuhan 430070, Hubei, P. R. China. E-mail: mlq518@whut.edu.cn
[b]Department of Chemistry, University of California, Berkeley, CA 94702, USA
[c]School of New Materials and New Energies, Shenzhen Technology University, Shenzhen 518118, P. R. China. E-mail: hanyulai@sztu.edu.cn
[d]School of Applied Technology, Shenzhen University, Shenzhen 518118, P. R. China

† Electronic supplementary information (ESI) available. See DOI: 10.1039/c7ta07024a

and the –CN functional groups in PAN fibers enable *in situ* N-doping into the fibers during carbonization.[41] Meanwhile, electrospinning technique is an advanced method to generate one dimensional (1D) PAN nanofibers[42–44] extruded from a polymer solution *via* high electrostatic forces,[45] from which we can obtain freestanding electrode materials based on PAN nanofiber networks. This approach effectively avoids addition of a metal current collector, conductive additive and binder, which are commonly used in the preparation of traditional electrodes. In this study, MgO is employed as a hard template to prepare porous carbon fibers with N-doping due to its low cost and easy removal, which can avoid the application of some expensive hard templates,[46] complicated activation,[16] and aggressive chemicals.[47] Furthermore, this method makes the scale-up synthesis of porous carbon fibers possible. N-MCNFs synthesized by carbonization at 900 °C (N-MCNFs-900) are applied as the electrode of supercapacitors, which exhibits a high specific capacitance up to 327.3 F g^{-1} at a current density of 1 A g^{-1}, and displays outstanding rate capability and long cycling stability.

2. Results and discussion

The synthetic procedure of the flexible freestanding N-MCNF electrode involves the following steps, as schematically illustrated in Fig. 1(a) and (b). Firstly, PAN/$Mg(OH)_2$/*N*,*N*-dimethylformamide (DMF) solution was electrospun into nanofibers. Then, the electrospun nanofiber network was pre-oxidized at 280 °C under air, aiming to obtain dimensional stability of the carbon nanofibers. Afterward, the nanofiber network was carbonized at 900 °C under a nitrogen flow atmosphere. These two steps were accompanied by a change in the colour of the sample from white to dark-brown, and then to black (Fig. S1, ESI†), and a black carbon nanofiber network was obtained. The final step is an acid treatment *via* HCl aqueous solution to remove the MgO template, and mesopores were formed in the carbon nanofibers. After etching the MgO template, the flexible freestanding N-MCNFs-900 network electrode material was fabricated (Fig. 1(c) and (d)). For comparison, a control experiment was also carried out without $Mg(OH)_2$ in the initial solutions, and the as-prepared carbon nanofibers are denoted as CNFs-900.

The $Mg(OH)_2$ nanoplates synthesized through a reflux method were used as the starting material. The crystallographic structure, morphology and composition of $Mg(OH)_2$ nanoplates are characterized by X-ray diffraction (XRD), field emission scanning electron microscopy (FESEM), thermogravimetric analysis (TGA) and derivative thermogravimetric analysis (DTG) tests. As shown in the XRD pattern of the $Mg(OH)_2$ nanoplates (Fig. S2, ESI†), the sample can be indexed as a pure phase in

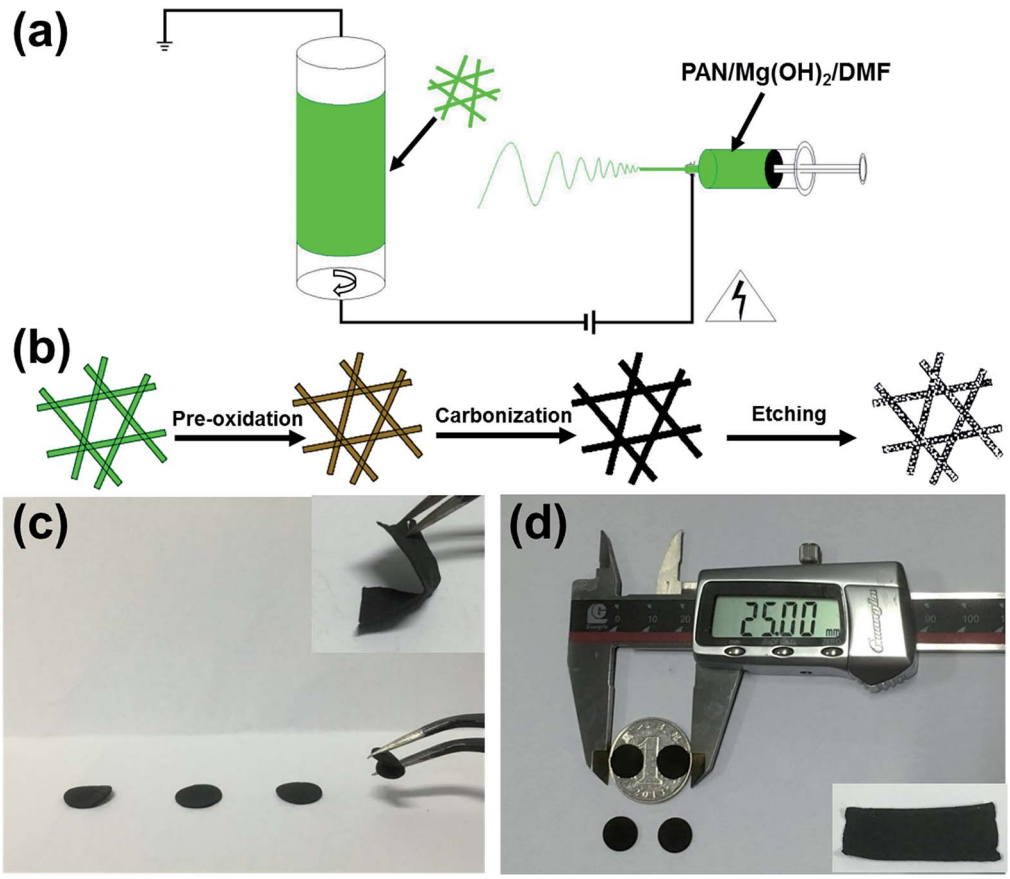

Fig. 1 (a, b) Schematic illustration of the experimental procedures to synthesize the flexible electrode. (c, d) Photograph of the flexible freestanding electrodes.

good agreement with the standard pattern (JCPDS card No. 44-1482). The FESEM image shows that these $Mg(OH)_2$ nanoplates are highly uniform with an average size of about 100 nm (Fig. S3(a), ESI†), and the thickness of the nanoplates is determined to be about 10 nm (Fig. S3, ESI†). TGA and DTG curves of the $Mg(OH)_2$ are demonstrated in Fig. S4 (ESI†), which shows that the total weight loss of the sample after the annealing treatment is approximately 31.8%. From the DTG curve, it is obvious that the rate of weight loss is highest when the temperature increases to 392.1 °C, which could be attributed to the decomposition of the $Mg(OH)_2$ into MgO and H_2O. The standard enthalpies of formation (ΔH_f^0) at 298.15 K of $Mg(OH)_2$, MgO and H_2O are −924.5, −601.7 and −285.8 kJ mol^{-1}, respectively. The calculated standard enthalpy of the reaction (ΔH^0) at 298.15 K is 37.0 kJ mol^{-1}.[48] The weight loss of 31.8% corresponds well with the calculated weight loss (30.9%) of this reaction.

Next, FESEM was employed to characterize the precursor fibers and their corresponding calcination products. Fig. 2 shows the morphological characterization of the $Mg(OH)_2$-free PAN nanofibers, PAN/$Mg(OH)_2$ nanofibers, and mesoporous nanofibers. As shown in Fig. 2(a), the $Mg(OH)_2$-free PAN nanofibers have smooth surfaces with an average diameter of about 500 nm and lengths up to several hundreds of millimeters. Fig. 2(b) exhibits the typical FESEM image of the initial PAN/$Mg(OH)_2$ nanofibers with a diameter of about 500 nm and a very smooth surface, which are ultralong and uniform (Fig. S5, ESI†). Moreover, the nanofibers are well interconnected with each other to form a three-dimensional (3D) open architecture. During carbonization, the morphology of PAN/$Mg(OH)_2$ nanofibers is perfectly preserved, but the diameter becomes narrower due to the volume shrinkage of PAN and weight loss of $Mg(OH)_2$. Fig. 2(c) reveals rough surfaces of carbon with uniform fibrous morphology after carbonization, which can be attributed to the *in situ* crystallization of magnesium ions into the MgO crystals. Meanwhile, PAN was carbonized into an amorphous carbon framework, as confirmed by the XRD pattern (Fig. S6, ESI†). Before acid treatment, the nanofibers were filled with the opaque MgO, as shown in the energy dispersive spectroscopy (EDS) characterization results (Fig. 2(d–f)). The EDS elemental mapping images reveal that Mg and O elements are homogeneously distributed in the nanofibers. The FESEM, transmission electron microscopy (TEM), and high-resolution TEM (HRTEM) images of the samples after acid treatment are shown in Fig. 2(g–i). After etching the MgO using HCl aqueous solution, the uniform mesoporous structure in the carbon matrix can be clearly observed from FESEM (Fig. 2(g)) and low-resolution TEM images (Fig. 2(h)). Moreover, in the HRTEM image, many micropores are observed. Obviously, no lattice fringes of carbon can be observed in the HRTEM image (Fig. 2(i)), indicating the amorphous nature of carbon in N-MCNFs-900. The corresponding selected area electron diffraction (SAED) pattern shows diffuse scattering (inset in Fig. 2(i)), demonstrating that the synthesized N-MCNFs-900 is amorphous.

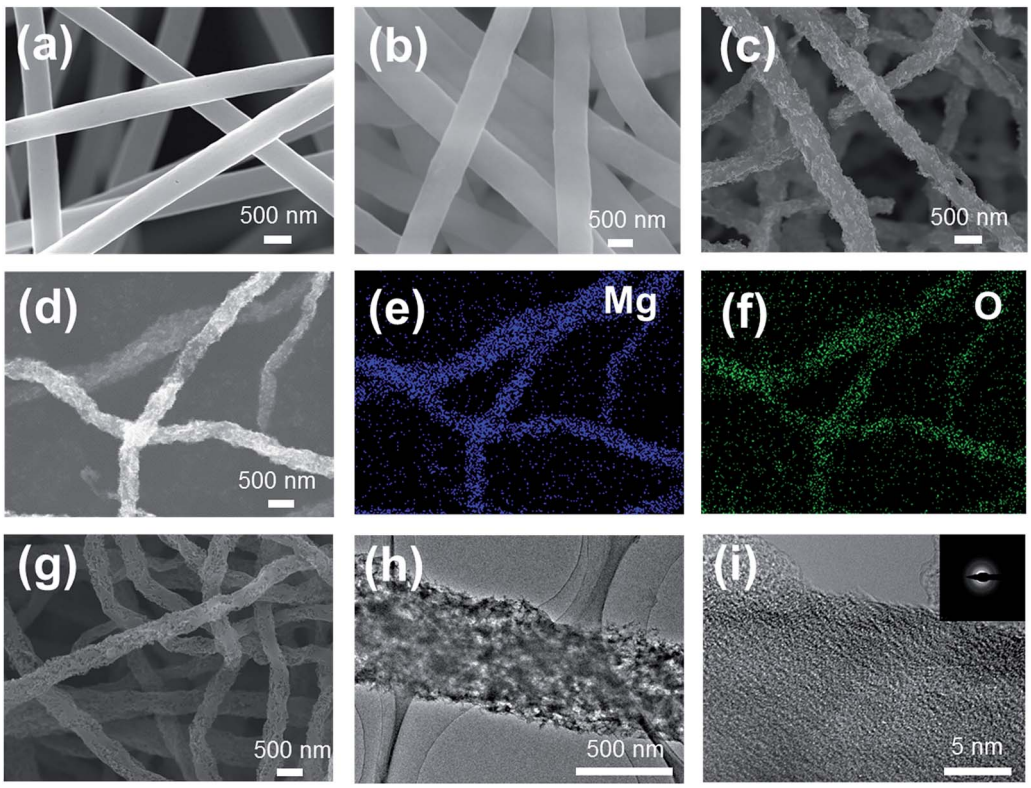

Fig. 2 FESEM images of (a) PAN nanofibers, (b) PAN/$Mg(OH)_2$ composite nanofibers and (c) PAN/$Mg(OH)_2$ nanofibers by carbonization at 900 °C. (d–f) EDS elemental mapping images of the PAN/$Mg(OH)_2$ nanofibers after carbonization at 900 °C. (g) FESEM image of N-MCNFs-900. (h) Low-magnification TEM image and (i) HRTEM image of N-MCNFs-900 (inset: SAED pattern).

The XRD pattern displays broad characteristic peaks at 2 theta values of about 25° and 43° of N-MCNFs-900 and CNFs-900 in Fig. 3(a). The two peaks can be assigned to the (002) and (101) diffraction of the hexagonal carbon material (JCPDS card No. 75-1621),[26] indicating the crystalline nature of carbon with a very small particle size.[49] The samples were characterized *via* Raman spectroscopy. As shown in Fig. 3(b), the Raman spectra further provide more detailed information of CNFs-900 and N-MCNFs-900, both of which display two typical characteristic D (disorder) and G (graphite) peaks. The D band (1344 cm^{-1}) is related to disordered carbon, and the G band (1596 cm^{-1}) is assigned to the highly ordered graphite structure. The relative intensity ratio of the D and G peaks ($R = I_D/I_G$) in the Raman spectrum is applied to evaluate the amorphous degree, and it is known that a higher intensity ratio means a higher amorphous degree of the carbon. The values of R are 1.01 and 1.04 for N-MCNFs-900 and CNFs-900, respectively. The chemical composition of N-MCNFs-900 is 76.15 wt% C, 11.55 wt% O and 6.5 wt% N, which were characterized using a CHON elemental analyzer (Table S1, ESI†), showing a high content of oxygen and nitrogen functional groups in the nanofibers. In order to confirm whether the MgO template was completely removed, the thermal behaviour of the N-MCNFs-900 and CNFs-900 was examined in air. Noticeably, there is negligible residual weight in the TGA curve of N-MCNFs-900, demonstrating that the MgO template was removed completely and pure N-MCNFs-900 was obtained after acid treatment (Fig. S7, ESI†). Afterward, surface analysis of N-MCNFs-900 was carried out by using X-ray photoelectron spectroscopy (XPS) (Fig. 3(c)). The C 1s, O 1s and N 1s peaks can be observed in the XPS survey spectrum, which is in good agreement with the results of elemental analysis (Table S1 (ESI†)). Obviously, N-doping from the decomposition of PAN is beneficial as it gives rise to defects and enhances the electrical conductivity of pyrolyzed carbon, resulting in the improvement of its electrochemical performance. The high-resolution N 1s spectrum (Fig. 3(d)) could be divided into three characteristic peaks at 398.2, 399.8 and 401.0 eV, corresponding to the three types of nitrogen functional groups, *i.e.* N-6, N-5 and N-Q, respectively.[15,50,51] Fig. 3(e) schematically illustrates the three types of nitrogen configurations. Among the three types of commonly observed structures of N-dopant atoms, N-6 and N-5 could offer more active sites to enhance the pseudocapacitance, resulting in improvement in the power density of supercapacitors.[15,21,52]

In addition to the unique mesoporous nanostructure, the wettability of N-MCNFs-900 is also quite interesting. Dynamic water contact angle measurements were performed for the samples as illustrated in Fig. 4. For comparison, the results for CNFs-900 are also presented. Generally, pure carbon materials are highly hydrophobic, preventing water from getting into small pores, which limits the effective surface area of the electrode material. Interestingly, different wetting processes were observed for N-MCNFs-900 and CNFs-900. N-MCNFs-900 is quite hydrophilic, but CNFs-900 is highly hydrophobic with the initial contact angle of 137.9°, which remains almost unchanged for 30 s or longer. The results indicate that the wettability of N-MCNFs-900 for water is better than that of CNFs-900.

It is well known that the SSA and pore size distribution (PSD) of the electrode materials play a prominent role in the electrochemical performance of supercapacitors.[53] Therefore, Brunauer–Emmett–Teller (BET) and Barrett–Joyner–Halenda (BJH) tests of the samples were conducted. For comparison, CNFs-900 was treated under the same conditions as N-MCNFs-900, and the N_2 adsorption–desorption isotherms of the samples are shown in Fig. 5. A remarkable hysteresis loop of the typical type-IV curve at relative pressure (P/P_0) ranging from 0.8 to 1.0 was

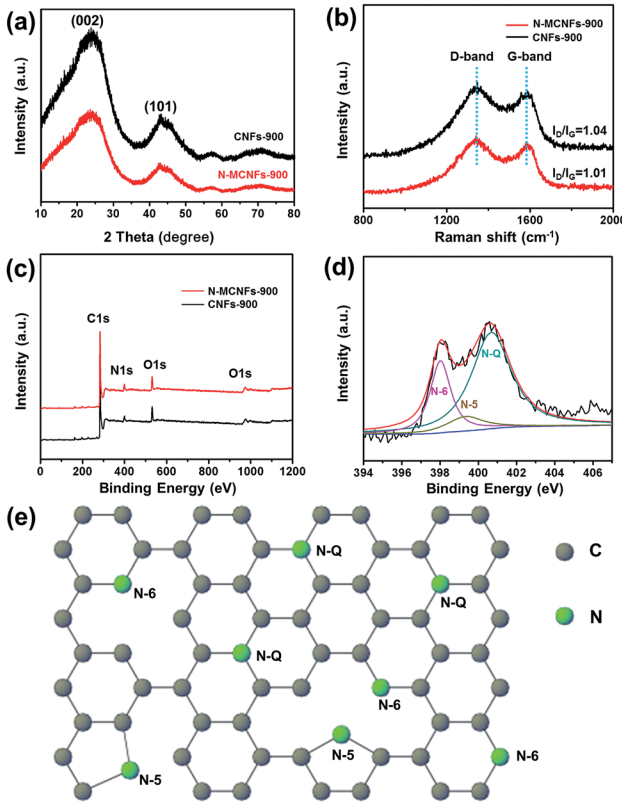

Fig. 3 (a) XRD patterns of N-MCNFs-900 and CNFs-900. (b) Raman spectra of N-MCNFs-900 and CNFs-900. (c) XPS survey spectra of N-MCNFs-900 and CNFs-900. (d) High-resolution XPS spectra of the N 1s peak of N-MCNFs-900. (e) Possible locations for N incorporation into the mesoporous carbon network.

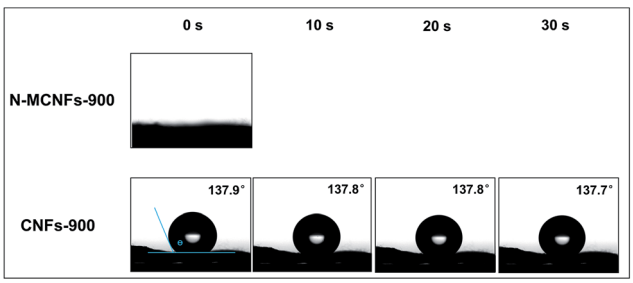

Fig. 4 Dynamic water contact angle measurements for N-MCNFs-900 and CNFs-900. The photograph at 0 s was taken immediately after resting the water droplet on the surface.

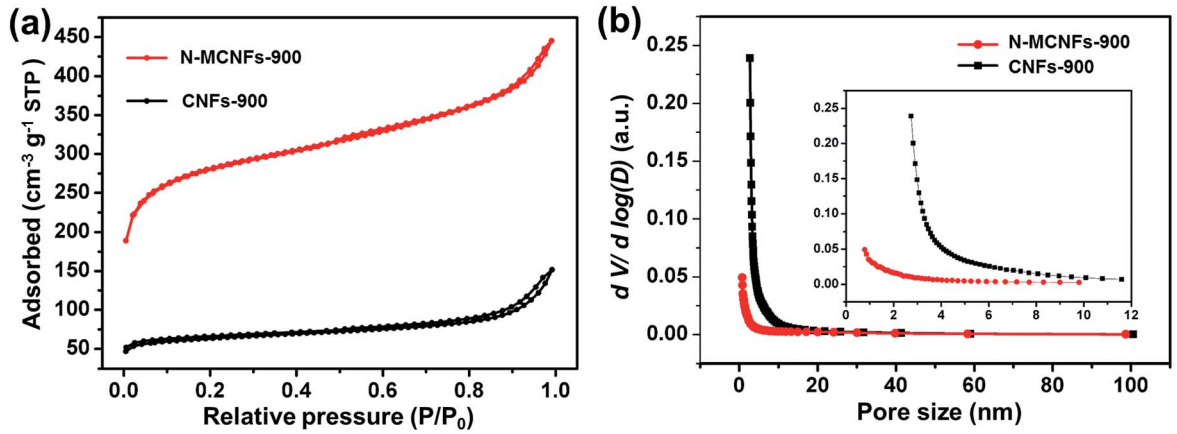

Fig. 5 (a) N_2 adsorption–desorption isotherms and (b) PSD of N-MCNFs-900 and CNFs-900.

observed, indicating that the N-MCNFs-900 sample exhibits a typical mesoporous feature. The PSD curves show that the size of the pores mainly falls in the range of 2 to 4 nm. The SSA of the N-MCNFs-900 sample was estimated to be 926.40 $m^2 g^{-1}$, which is much higher than those of the previously reported porous CNFs.[16,54,55] It is worth noting that only low SSA (208.03 $m^2 g^{-1}$) was observed for CNFs-900 (Table S2, ESI†). Therefore, these results indicate the importance of the introduction of $Mg(OH)_2$ into the nanofibers, which not only acts as the structural constructor and *in situ* porogen, but also improves the SSA of N-MCNFs-900.

The aforementioned results indicate that the *in situ* MgO template method provides a unique architecture of N-MCNFs-900 with good wettability and high SSA, which satisfies the general demands of ideal EDLC electrode materials. To evaluate the supercapacitive performance of N-MCNFs-900, herein we constructed a traditional three-electrode configuration in 6 M KOH liquid electrolyte to measure the electrochemical performance of the electrodes. Cyclic voltammetry (CV) and galvanostatic charge/discharge (GCD) measurements were performed. Firstly, CV measurements were conducted at various scan rates (Fig. 6 and 7(a)). As shown in CV curves, the remarkable difference in the electrochemical performance of N-MCNFs-900 and CNFs-900 could be obviously recognized. Typically, rectangular shapes of the CV curves are obtained even at a very high scan rate of 500 mV s^{-1}, indicating a very fast and efficient charge transfer, which confirms that N-MCNFs-900 and CNFs-900 possess a highly capacitive nature and a small equivalent

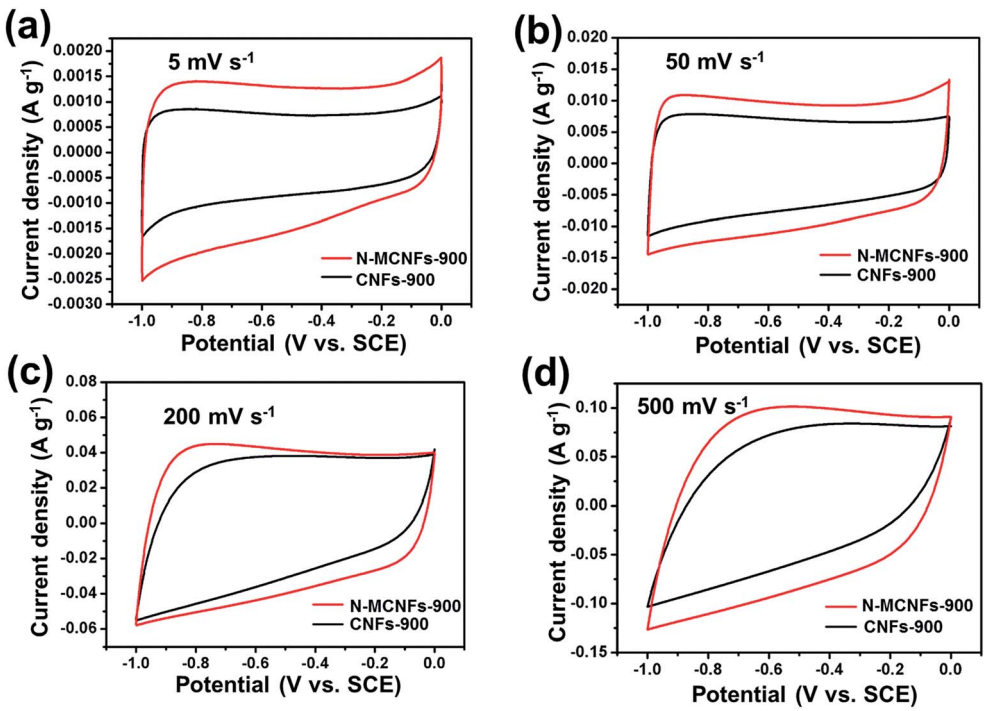

Fig. 6 CV curves of N-MCNFs-900 and CNFs-900 at scan rates of (a) 5 mV s^{-1}, (b) 50 mV s^{-1}, (c) 200 mV s^{-1}, and (d) 500 mV s^{-1}.

series resistance (ESR) with rapid charge–discharge. It is worth noting that CNFs-900 also exhibits rather good capacitive behaviour, but is obviously inferior to that of N-MCNFs-900.

To further investigate the electrochemical performance of the synthesized samples, the capacitances of N-MCNFs-900 and CNFs-900 were studied by GCD (Fig. 7(b) and S9, ESI†), which is an accurate technique to evaluate the electrochemical performance of supercapacitor electrodes. The typical GCD curves of N-MCNFs-900 exhibit highly symmetric and nearly linear slopes, and rather limited voltage (*IR*) drops even at a high current density of 20 A g^{-1} (Fig. 7(c)), which also indicates the ideal capacitive behaviour. From GCD curves in Fig. 7(d), it was found that N-MNFs-900 has a specific capacitance as high as 327.3, 301.4, 260.6, 244.3 and 224.1 F g^{-1} at the discharge current density of 1, 2, 5, 10 and 20 A g^{-1}, respectively, which could be highly competitive among carbon-based materials. Even at a high current density of 20 A g^{-1}, N-MNFs-900 still maintains a high specific capacitance of 224.1 F g^{-1}, ~68% of its initial capacitance, showing outstanding rate capability. Such superior rate capability is ascribed to the unique mesoporous architecture, which can offer an efficient pathway for the electrolyte ions through the carbon framework.[56] Importantly, N-MCNFs-900 exhibits superior cycling stability of about 93% capacitance retention after 10 000 cycles at a high current density of 20 A g^{-1} with coulombic efficiency of about 100% (Fig. 7(e)), which is especially desirable in supercapacitors.

In order to clearly elucidate the excellent performance of the prepared *in situ* N-doped mesoporous carbon materials, we compared our results with some reported results on N-doped porous carbon materials. To the best of our knowledge, representative characteristics, such as precursors, electrolytes, current density and capacitance, are listed in Table S3 (ESI†); the capacitance of the as-obtained N-MCNFs-900 is much higher than that of most reported carbon-based electrodes. Between the two samples N-MCNFs-900 and CNFs-900, the better electrochemical performance of N-MCNFs-900 is ascribed to its larger SSA, uniform pore size distribution, the high degree of heteroatom doping (nitrogen content: 6.48 wt%, oxygen content: 11.55 wt%) and higher electrical conductivity, which result in the fast transport of ions and electrons and a large space for charge storage.[26] The excellent electrochemical performance of the asymmetric N-MCNFs-900 supercapacitor might be attributed to the following aspects: (1) 1D mesoporous nanofibers can provide short pathways for electron/ion transport and accessible penetration of the electrolyte, which was verified by the result of electrochemical impedance spectroscopy (EIS) (Fig. 7(f)); the width of the semicircle impedance loop in the high frequency region reflects the resistance to mass transfer/diffusion rate of ions; (2) the 3D network structure combined with the advantages of the N-MCNFs prepared by the *in situ* MgO template method, such as the large SSA, suitable pore structure and high electrical conductivity, which ensures the sufficient free space for charge storage and the fast transport of ions and electrons at the electrode/electrolyte interface; (3) the C–N bonds were introduced to improve the wettability and electrical conductivity by N-doping.[57] Besides EDLC, to some extent, the pseudocapacitance also contributes to the capacitance, which is derived from the effect of N-doping.[58–60] Moreover, N-doping in the composite effectively enhances the electrical conductivity and electrochemical reactivity, further improving the rate performance.[61]

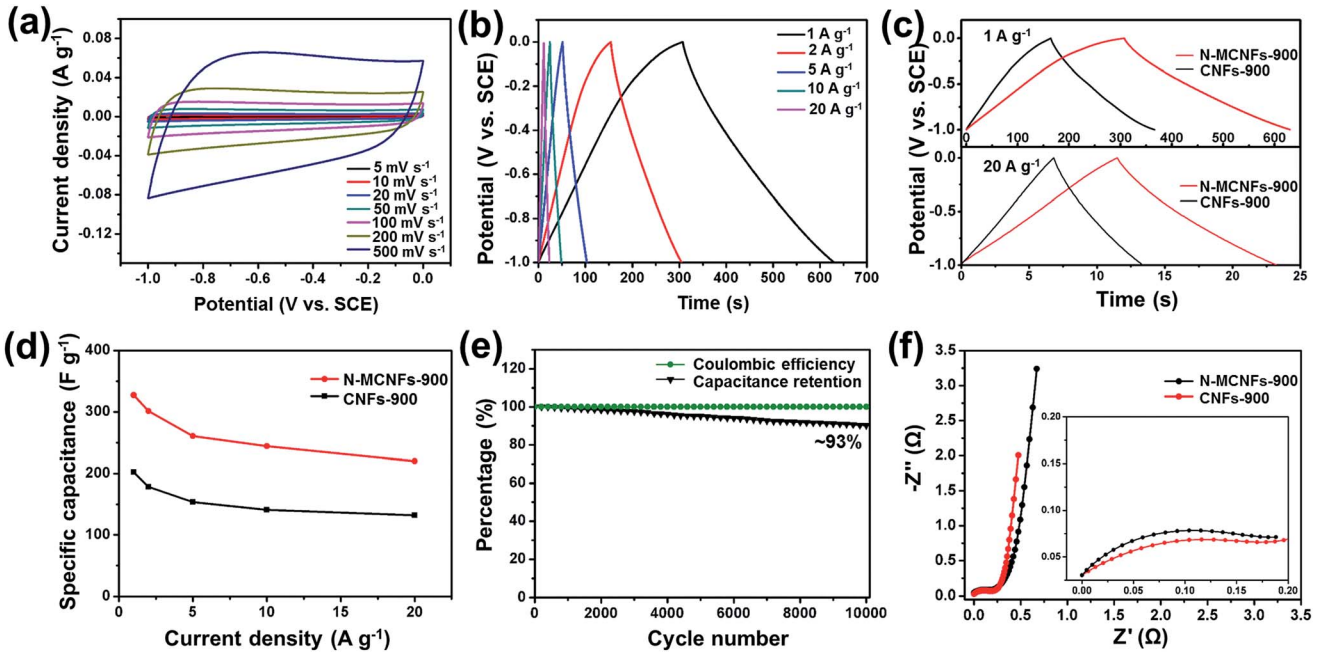

Fig. 7 Electrochemical performances of a freestanding carbon nanofiber electrode using a conventional three-electrode configuration in 6 M KOH aqueous electrolyte solution. (a) CV curves of N-MCNFs-900 at different scan rates of 5–500 mV s^{-1}. (b) GCD curves of N-MCNFs-900 at different current densities of 1, 2, 5, 10 and 20 A g^{-1}. (c) GCD curves of N-MCNFs-900 and CNFs-900 at the current densities of 1 and 20 A g^{-1}. (d) The specific capacitances calculated from the discharge curves at different current densities. (e) Cycling stability and coulombic efficiency of N-MCNFs-900 at a current density of 20 A g^{-1}. (f) Typical Nyquist plot of N-MCNFs-900 and CNFs-900.

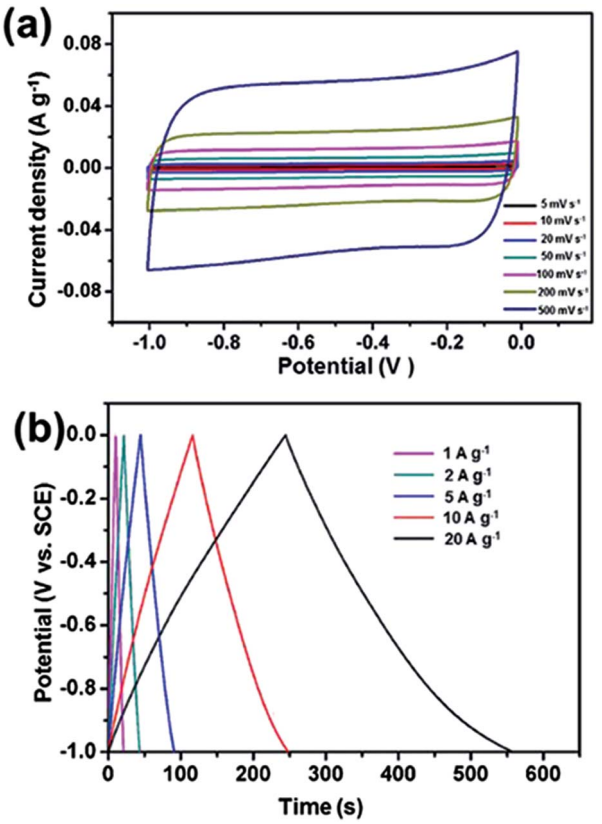

Fig. 8 (a) CV curves of N-MCNFs-900 at different scan rates in a two-electrode configuration using 6 M KOH electrolyte; (b) GCD curves of N-MCNFs-900 at different current densities in the two-electrode configuration using the 6 M KOH electrolyte.

To better illustrate the practical performance of N-MCNFs-900 and CNFs-900 carbonaceous electrode materials, we constructed a symmetric supercapacitor by using two pieces of N-MCNFs-900 with the same size and weight, tested in 6 M KOH electrolyte. As shown in Fig. 8(a) and S10(a) (ESI†), the CV curves exhibit quasi-rectangular shapes, and no redox peak appears even at a high scan rate. We also investigated the GCD (Fig. 8(b) and S10(b) (ESI†)) at different current densities in the range of 1–20 A g^{-1}, and the GCD curves show a symmetrical triangle with very small *IR* drop for each current density, indicating the reversible behaviour of an ideal supercapacitor. Calculated from the GCD (Fig. 8(b)) of N-MCNFs-900, at a current density of 1 A g^{-1}, the specific capacitance is maintained at 308.8 F g^{-1}, and the energy density is 42.5 W h kg^{-1} which is much higher than most values previously reported (Table S4, ESI†). Even at a high current density of 20 A g^{-1}, the specific capacitance still remains at 208 F g^{-1}, showing the good stability of the electrode. A more detailed comparison is summarized in Table S4 (ESI†), which further demonstrates the advantages of our N-MCNFs-900 over the reported N-doped porous carbon materials for SCs.

3. Conclusions

In summary, we have successfully designed and fabricated N-MCNFs as flexible freestanding electrodes for supercapacitors with *in situ* N-doping and an *in situ* MgO template through a single-nozzle electrospinning approach. The employed synthesis process of the $Mg(OH)_2$ nanoplates is low-cost, facile and environmentally friendly. The as-synthesized carbon nanofiber electrode with a unique mesoporous structure is a highly promising candidate for supercapacitors with a high capacity (327.3 F g^{-1} at a current density of 1 A g^{-1}), good rate capability (~68% of initial capacitance at a high current density of 20 A g^{-1}), and outstanding cycling stability (~93% capacitance retention 10 000 cycles). All these results indicate that the N-doped mesoporous carbon nanofibers are highly suitable for the advanced electrode materials of supercapacitors. This work provides a facile and green method to prepare mesoporous carbon materials, and opens new avenues for the exploration of other porous carbon-based materials. Meanwhile, this work displays attractive prospects and wide potential for other energy storage devices, such as lithium-ion batteries, sodium-ion batteries, lithium–sulfur batteries and metal–air batteries, which is of great significance.

Conflicts of interest

There are no conflicts to declare.

Acknowledgements

This work was supported by the National Key Research and Development Program of China (2016YFA0202603, 2016YFA0202604), the National Basic Research Program of China (2013CB934103), the National Natural Science Foundation of China (51521001, 51502227, and 51579198) and the Startup Foundation of Shenzhen Technology University (No. 201701). Prof. L. Q. M. gratefully acknowledges financial support from the China Scholarship Council (No. 201606955096).

Notes and references

1 S. Chu and A. Majumdar, *Nature*, 2012, **488**, 294–303.
2 L. Mai, X. Tian, X. Xu, L. Chang and L. Xu, *Chem. Rev.*, 2014, **114**, 11828.
3 D. Larcher and J. M. Tarascon, *Nat. Chem.*, 2015, **7**, 19–29.
4 L. Hu, J. W. Choi, Y. Yang, S. Jeong, F. L. Mantia, L. F. Cui, Y. Cui and C. M. Lieber, *Proc. Natl. Acad. Sci. U. S. A.*, 2009, **106**, 21490–21494.
5 J. R. Miller and P. Simon, *Science*, 2008, **321**, 651.
6 P. Simon and Y. Gogotsi, *Nat. Mater.*, 2008, **7**, 845–854.
7 L. Q. Mai, F. Yang, Y. L. Zhao, X. Xu, L. Xu and Y. Z. Luo, *Nat. Commun.*, 2011, **2**, 381.
8 M. Winter and R. J. Brodd, *Chem. Rev.*, 2004, **104**, 4245–4269.
9 M. Salanne, B. Rotenberg, K. Naoi, K. Kaneko, P. L. Taberna, C. P. Grey, B. Dunn and P. Simon, *Nat. Energy*, 2016, **1**, 16070.
10 B. E. Conway, *Electrochemical Supercapacitors-Scientific Fundamentals and Technological Applications*, Kluwer Academic, New York, 1999.
11 M. D. Stoller and R. S. Ruoff, *Energy Environ. Sci.*, 2010, **3**, 1294–1301.

12 A. Izadi-Najafabadi, D. N. Futaba, S. Iijima and K. Hata, *J. Am. Chem. Soc.*, 2010, **132**, 18017–18019.
13 T. Lin, I. W. Chen, F. Liu, C. Yang, H. Bi, F. Xu and F. Huang, *Science*, 2015, **350**, 1508–1513.
14 J. Gamby, P. L. Taberna, P. Simon, J. F. Fauvarque and M. Chesneau, *J. Power Sources*, 2001, **101**, 109–116.
15 L. F. Chen, X. D. Zhang, H. W. Liang, M. Kong, Q. F. Guan, P. Chen, Z. Y. Wu and S. H. Yu, *ACS Nano*, 2012, **6**, 7092–7102.
16 C. Kim, B. T. N. Ngoc, K. S. Yang, M. Kojima, Y. A. Kim, Y. J. Kim, M. Endo and S. C. Yang, *Adv. Mater.*, 2007, **19**, 2341–2346.
17 M. Kaempgen, C. K. Chan, J. Ma, Y. Cui and G. Gruner, *Nano Lett.*, 2009, **9**, 1872–1876.
18 K. Wang, Q. Meng, Y. Zhang, Z. Wei and M. Miao, *Adv. Mater.*, 2013, **25**, 1494–1498.
19 J. Han, G. Xu, B. Ding, J. Pan, H. Dou and D. R. Macfarlane, *J. Mater. Chem. A*, 2014, **2**, 5352–5357.
20 Q. Li, R. Jiang, Y. Dou, Z. Wu, T. Huang, D. Feng, J. Yang, A. Yu and D. Zhao, *Carbon*, 2011, **49**, 1248–1257.
21 W. Li, D. Chen, Z. Li, Y. Shi, Y. Wan, J. Huang, J. Yang, D. Zhao and Z. Jiang, *Electrochem. Commun.*, 2007, **9**, 569–573.
22 J. C. Lytle, J. M. Wallace, M. B. Sassin, A. J. Barrow, J. W. Long, J. L. Dysart, C. H. Renninger, M. P. Saunders, N. L. Brandell and D. R. Rolison, *Energy Environ. Sci.*, 2011, **4**, 1913–1925.
23 J. Zhao, Y. Jiang, H. Fan, M. Liu, O. Zhuo, X. Wang, Q. Wu, L. Yang, Y. Ma and Z. Hu, *Adv. Mater.*, 2017, **29**, 1604569.
24 D. Hulicova-Jurcakova, M. Seredych, G. Q. Lu and T. J. Bandosz, *Adv. Funct. Mater.*, 2009, **19**, 438–447.
25 D. Hulicova-Jurcakova, M. Kodama, S. Shiraishi, H. Hatori, Z. H. Zhu and G. Q. Lu, *Adv. Funct. Mater.*, 2009, **19**, 1800–1809.
26 F. Su, C. K. Poh, J. S. Chen, G. Xu, D. Wang, Q. Li, J. Lin and X. W. Lou, *Energy Environ. Sci.*, 2010, **4**, 717–724.
27 Z. Li, Z. Xu, X. Tan, H. Wang, C. M. B. Holt, T. Stephenson, B. C. Olsen and D. Mitlin, *Energy Environ. Sci.*, 2013, **6**, 871–878.
28 D. W. Wang, F. Li, Z. G. Chen, G. Q. Lu and H. M. Cheng, *Chem. Mater.*, 2008, **20**, 7195–7200.
29 E. Rodríguez, I. Cameán, R. García and A. B. García, *Electrochim. Acta*, 2011, **56**, 5090–5094.
30 Y. Li, G. Wang, T. Wei, Z. Fan and P. Yan, *Nano Energy*, 2016, **19**, 165–175.
31 H.-K. Jeong, M. Jin, E. J. Ra, K. Y. Sheem, G. H. Han, S. Arepalli and Y. H. Lee, *ACS Nano*, 2010, **4**, 1162–1166.
32 D. Hulicova-Jurcakova, A. M. Puziy, O. I. Poddubnaya, F. Suárez-García, J. M. D. Tascón and G. Q. Lu, *J. Am. Chem. Soc.*, 2009, **131**, 5026–5027.
33 X. Li, H. Wang, J. T. Robinson, H. Sanchez, G. Diankov and H. Dai, *J. Am. Chem. Soc.*, 2009, **131**, 15939–15944.
34 A. L. Reddy, A. Srivastava, S. R. Gowda, H. Gullapalli, M. Dubey and P. M. Ajayan, *ACS Nano*, 2010, **4**, 6337–6342.
35 R. Lv, T. Cui, M.-S. Jun, Q. Zhang, A. Cao, D. S. Su, Z. Zhang, S.-H. Yoon, J. Miyawaki, I. Mochida and F. Kang, *Adv. Funct. Mater.*, 2011, **21**, 999–1006.
36 N. D. Kim, W. Kim, J. B. Joo, S. Oh, P. Kim, Y. Kim and J. Yi, *J. Power Sources*, 2008, **180**, 671–675.
37 L. L. Zhang, X. Zhao, H. Ji, M. D. Stoller, L. Lai, S. Murali, S. Mcdonnell, B. Cleveger, R. M. Wallace and R. S. Ruoff, *Energy Environ. Sci.*, 2012, **5**, 9618–9625.
38 Y. Chen, X. Li, K. Park, L. Zhou, H. Huang, Y. W. Mai and J. B. Goodenough, *Angew. Chem., Int. Ed.*, 2016, **55**, 15831–15834.
39 X. Li, Y. Chen, H. Huang, Y. W. Mai and L. Zhou, *Energy Storage Mater.*, 2016, **5**, 58–92.
40 H. Wu, G. Chan, J. W. Choi, I. Ryu, Y. Yao, M. T. McDowell, S. W. Lee, A. Jackson, Y. Yang, L. Hu and Y. Cui, *Nat. Nanotechnol.*, 2012, **7**, 310–315.
41 Y. Chen, X. Li, K. Park, J. Song, J. Hong, L. Zhou, Y. W. Mai, H. Huang and J. B. Goodenough, *J. Am. Chem. Soc.*, 2013, **135**, 16280–16283.
42 L. Zhang, Y. Huang, Y. Zhang, H. Gu, W. Fan and T. Liu, *Adv. Mater. Interfaces*, 2016, **3**, 1500467.
43 D. Li and Y. Xia, *Adv. Mater.*, 2004, **16**, 1151–1170.
44 E. J. Ra, E. Raymundo-Piñero, Y. H. Lee and F. Béguin, *Carbon*, 2009, **47**, 2984–2992.
45 Y. M. Shin, M. M. Hohman, M. P. Brenner and G. C. Rutledge, *Polymer*, 2001, **42**, 09955–09967.
46 F. Goettmann, A. Fischer, M. Antonietti and A. Thomas, *Angew. Chem., Int. Ed.*, 2006, **45**, 4467–4471.
47 M. Steinhart, C. Liang, G. W. Lynn, U. Gosele and S. Dai, *Chem. Mater.*, 2007, **19**, 2383–2385.
48 S. Makhluf, R. Dror, Y. Nitzan, Y. Abramovich, R. Jelinek and A. Gedanken, *Adv. Funct. Mater.*, 2005, **15**, 1708–1715.
49 F. Zheng, Y. Yang and Q. Chen, *Nat. Commun.*, 2014, **5**, 5261.
50 F. Su, C. K. Poh, J. S. Chen, G. Xu, D. Wang, Q. Li, J. Lin and X. W. Lou, *Energy Environ. Sci.*, 2011, **4**, 717–724.
51 L. F. Chen, Z. H. Huang, H. W. Liang, W. T. Yao, Z. Y. Yu and S. H. Yu, *Energy Environ. Sci.*, 2013, **6**, 3331–3338.
52 C. Ma, X. Shao and D. Cao, *J. Mater. Chem.*, 2012, **22**, 8911–8915.
53 C. Merlet, B. Rotenberg, P. A. Madden, P.-L. Taberna, P. Simon, Y. Gogotsi and M. Salanne, *Nat. Mater.*, 2012, **11**, 306–310.
54 L.-F. Chen, Y. Lu, L. Yu and X. W. Lou, *Energy Environ. Sci.*, 2017, **10**, 1777–1783.
55 J. T. McCann, M. Marquez and Y. Xia, *J. Am. Chem. Soc.*, 2006, **128**, 1436–1437.
56 Y. Liang, D. Wu and R. Fu, *Langmuir*, 2009, **25**, 7783.
57 J. Zhao, H. Lai, Z. Lyu, Y. Jiang, K. Xie, X. Wang, Q. Wu, L. Yang, Z. Jin and Y. Ma, *Adv. Mater.*, 2015, **27**, 3541–3545.
58 Z. S. Wu, A. Winter, L. Chen, Y. Sun, A. Turchanin, X. Feng and K. Müllen, *Adv. Mater.*, 2012, **24**, 5130–5135.
59 Z. Wen, X. Wang, S. Mao, Z. Bo, H. Kim, S. Cui, G. Lu, X. Feng and J. Chen, *Adv. Mater.*, 2012, **24**, 5610–5616.
60 Z. Li, L. Zhang, B. S. Amirkhiz, X. Tan, Z. Xu, H. Wang, B. C. Olsen, C. M. B. Holt and D. Mitlin, *Adv. Energy Mater.*, 2012, **2**, 431–437.
61 L. Qie, W. M. Chen, Z. H. Wang, Q. G. Shao, X. Li, L. X. Yuan, X. L. Hu, W. X. Zhang and Y. H. Huang, *Adv. Mater.*, 2012, **24**, 2047–2050.